Onset of electroconvection of homeotropically aligned nematic liquid crystals

Sheng-Qi Zhou,[1] Nándor Éber,[2] Ágnes Buka,[2] Werner Pesch,[3] and Guenter Ahlers[1]
[1]*Department of Physics and iQCD, University of California, Santa Barbara, California 93106, USA*
[2]*Research Institute for Solid State Physics and Optics, H-1525 Budapest P.O. Box 49, Hungary*
[3]*Physikalisches Institut der Universität Bayreuth, D-95440 Bayreuth, Germany*
(Received 9 February 2006; published 19 October 2006)

We present experimental measurements near the onset of electroconvection (EC) of homeotropically aligned nematic liquid crystals Phase 5A and MBBA. A voltage of amplitude $\sqrt{2}V_0$ and frequency f was applied. With increasing V_0, EC occurred after the bend Freedericksz transition. We found supercritical bifurcations to EC that were either stationary bifurcations or Hopf bifurcations to traveling convection rolls, depending on the sample conductances. Results for the onset voltages V_c, the critical wave numbers k_c, the obliqueness angles θ_c, and the traveling-wave (Hopf) frequencies at onset ω_c over a range of sample conductances and driving frequencies are presented and compared, to the extent possible, with theoretical predictions. For the most part good agreement was found. However, the experiment revealed some unusual results for the orientations of the convection rolls relative to the direction selected by the Freedericksz domain.

DOI: 10.1103/PhysRevE.74.046211 PACS number(s): 47.54.−r, 47.20.−k, 47.20.Ky

I. INTRODUCTION

Whereas Rayleigh-Bénard convection in a thin horizontal layer of fluid heated from below [1] has been a paradigm in the study of pattern formation in systems with rotational symmetry, electroconvection (EC) in nematic liquid crystals (NLC's) has played that role for anisotropic systems [2–8] with a preferred direction in the plane of the sample. NLC molecules have an inherent orientational order, but no positional order, and the direction $\hat{\mathbf{n}}$ parallel to the average molecular alignment is referred to as the director [9,10]. The uniaxial symmetry of nematics is reflected in the anisotropy of the material properties—for instance, in different values of the electrical conductivities parallel ($\sigma_\parallel$) and perpendicular ($\sigma_\perp$) to the local director orientation. By confining the NLC's between two parallel glass plates, one can obtain an EC cell with either uniform planar (parallel to the surfaces) or uniform homeotropic (perpendicular to the surfaces) alignment of $\hat{\mathbf{n}}$. The case that prevails depends on the particular NLC and on the treatment of the confining glass surfaces. When the glass plates are covered on the inside by conducting electrodes, a voltage $V=\sqrt{2}V_0\cos(2\pi ft)$ can be applied to the sample. This will, for a wide range of material properties, induce convection when $V_0>V_c$. Thus at V_c a bifurcation occurs from a state that is spatially uniform in the plane of the nematic layer to a periodic array of convection rolls—i.e., to a pattern. Numerous experimental investigations have been devoted during the last two decades to the study of a richness of bifurcation and pattern-formation phenomena [11–26]. Unique to these anisotropic systems is the existence of oblique-roll patterns whose wave vector forms a nonzero angle θ with respect to the in-plane director (or more precisely with respect to the projection of $\hat{\mathbf{n}}$ on the plane parallel to the electrodes). Because the director is not a vector, the states with angles θ and $\pi-\theta$ are expected to be degenerate and are referred to as zig and zag rolls. At onset the structures can be stationary or traveling, depending on sample properties. A great variety of spatiotemporal structures is observed, including defect chaos and chaos at onset.

In parallel to this experimental work, truly remarkable theoretical progress occurred, primarily due to the Bayreuth group of Kramer and co-workers. Here we cite only some of the major theoretical milestones [27–29]; much else can be found in a number of reviews [2–6]. Many of the complex phenomena observed in experiments are now understood quantitatively.

For the homeotropic case the thermodynamic state, which prevails at small applied voltages, is rotationally invariant. This symmetry is broken at a thermodynamic phase transition that occurs at a voltage $V_0=V_F$ and that is known as the Freedericksz transition. There the director in the sample interior develops a nonzero component n_x in the plane of the sample. The transition to EC then follows at a larger voltage $V_c>V_F$. It has received somewhat less attention in the past than the transition to EC in samples with planar alignment. In this paper we examine the onset of EC in homeotropic samples for the two NLC's MBBA and Merck Phase 5A in greater detail than has been done before. We first discuss results for the Freedericksz transition and for the in-plane director orientation above it. The primary purpose of this is to provide information about the homogeneity of our samples above V_F where EC first occurs and to determine the direction of symmetry breaking by the Freedericksz domain. We then present results for the EC onset voltage V_c, the critical wave number k_c, the obliqueness angle θ_c, and the traveling-wave (Hopf) frequency at onset, ω_c, over a range of sample conductances $\sigma_\parallel$ and drive frequencies f. Our results expand the findings of Richter *et al.* [19,30], Tóth *et al.* [31], and Buka *et al.* [5] to larger parameter ranges. To the extent possible comparison with theoretical predictions by Hertrich *et al.* [28] will be made. Generally the agreement is remarkably good, although some discrepancies do remain for the magnitude of the wave vector of the convection rolls. Perhaps more interesting is that the experiment reveals some unusual features of the orientation of the convection rolls relative to the direction selected by the Freedericksz domain. It seems likely that this phenomenon is associated with the soft Goldstone mode [2,3,28], characteristic of this system,

but to our knowledge the details of this phenomenon remain unexplained at this time.

The origin of *homeotropic* EC is in principle well understood on the basis of the theoretical analysis of Hertrich *et al.* [28]. This analysis shows that the in-plane director component n_x at the midplane grows quickly above the Freedericksz transition at $V_0=V_F$. For instance, already at $V_0 \simeq 1.1V_F$ a planar layer with a thickness close to half the sample thickness d has developed. Consequently the standard Helfrich mechanism for *planar* convection is activated [32]. Thus it is expected that the main characteristics of EC in samples with planar alignment apply also to the homeotropic case.

The analysis of homeotropic EC [28] uses the "standard model" (SM) [2–6] which assumes that the sample is an Ohmic conductor and which does not capture Hopf bifurcations as observed in the present homeotropic samples as well as in several experiments with planar nematics. In the planar cases this discrepancy has been resolved by the introduction of the "weak electrolyte model" (WEM) [3,29,33] which takes into consideration the non-Ohmic nature of the conductance and the mobilities of the ions. WEM effects have not yet been considered in the homeotropic case [28]. Thus, in light of the discussion given above, we compared our measurements of the Hopf frequency ω_c with predictions of the WEM for the planar case. We find excellent agreement for the dependence of ω_c on the sample spacing and the conductance.

The rest of the paper is organized as follows. In Sec. II we describe the experimental details and the image-analysis methods. In Sec. III we discuss the Freedericksz transition and demonstrate that uniform large domains are obtained above it but below the onset of EC. The results for EC in Phase 5A and MBBA are presented in Sec. IV. There we first show that the bifurcation to EC is supercritical. We also give long-term results about the dependence of the onset voltage on time and briefly discuss the nature of the thermally induced fluctuations [34] near onset. Then we present the data for V_c, k_c, θ_c, and ω_c in that order in four subsections. A brief summary of the results is given in Sec. V.

II. EXPERIMENTAL PROCEDURE AND IMAGE ANALYSIS

The apparatus was nearly the same as the one described in Ref. [26]. It consisted of a shadowgraph system [35] with computer-controlled image acquisition, a temperature-controlled sample stage with a stability of 0.01 °C that contained the electroconvection cell, and electronics for applying the ac voltage and measuring the conductivity of the cell. The main new feature was that a mirror [36] had been added above the lower lens to change the light path from vertical to horizontal so that some optical components, including the camera lens and the charge-coupled-device (CCD) camera, could be fixed on an optical table. For the study of EC sometimes a single polarizer was used between the light source and the sample, but it had only a modest influence on the image contrast above onset at V_c.

The NLC's Merck Phase 5A and MBBA (*p*-methoxybenzylidene-*p*-butylaniline) were used. Phase 5A is a NLC mixture similar to Phase 5, except that it contains a dopant that enhances its conductivity. It was used at 30.00±0.01 °C in homeotropic cells that consisted of two parallel indium-tin-oxide- (ITO-) coated glass plates that had been extremely well cleaned but were not covered with any surface coating. The cell thickness and the parallel conductance $\sigma_\parallel$ are shown in Table I. For MBBA two types of homeotropic cells were prepared with different surface coatings. In one we used dimethyloctadecyl[3-(trimethoxysilyl)-propyl]ammonium chloride (DMOAP). In the other a special polyimide for homeotropic alignment [37] was applied. Measurements for MBBA were made at 25.00±0.01 °C. In order to get MBBA with different conductivities, it was doped with tetra-*n*-butyl-ammonium bromide (TBAB) in the range from 0 to 100 parts per million by weight. The cell thicknesses were measured with an interferometer [35] and are shown in Table I. There the conductances $\sigma_\parallel$ are given as well. Unless stated otherwise, the experimental description and results discussed are for the Phase 5A-1 and MBBA-4 cells. However, similar phenomena were found for the other cells.

TABLE I. Properties of the cells. The cell thickness d, parallel conductance $\sigma_\parallel$, surface coating, measured Freedericksz voltage V_F, and charge relaxation time $\tau_q=\epsilon_0\epsilon_\perp/\sigma_\perp$ are given. The last column shows the nature of the bifurcation to EC (H=Hopf, S=stationary). The theoretical prediction of $V_F^\infty=\pi\sqrt{k_{33}/(\epsilon_0|\epsilon_a|)}$, based on parameters from Refs. [38,28], is 8.76 V for Phase 5A and 4.25 V for MBBA.

Sample	d (μm)	$10^8\sigma_\parallel$ (Ω^{-1} m^{-1})	Surface coating	V_F (V)	$10^4\tau_q$ (s)	
Phase 5A-1	12.1	37	None	8.132	2.11	H
Phase 5A-2	12.0	31	None		2.52	H
MBBA-1	28.9	42	DMOAP	3.25	1.65	S
MBBA-2	34.4	16.6	DMOAP		4.20	S
MBBA-3	29.5	3.21	DMOAP	3.25	21.7	H
MBBA-4	41.8	5.55	Polyimide	3.90	12.6	H

We gained information about the quality of the homeotropic alignment by measuring the light intensity transmitted with zero applied voltage and two polarizers in the optical path, one before and another after the sample. With parallel polarizers there was nearly complete transmission, and with polarizers crossed at 90° there was nearly total extinction. Figure 1 shows the intensity ratio as a function of the angle of orientation, ϕ, of the crossed pair relative to the edges of the (rectangular) sample (the x and y axes). The open circles were obtained with no sample in place and show the extent of polarization of the light reflected from the mirror. One sees that all samples yielded results not far from the blank run, indicating that a good approximation to perfect homeotropic anchoring with very little pretilt was achieved in all cases.

At a fixed driving frequency f, we changed V_0 monotonically with nonequal steps; the steps became smaller near the estimated EC threshold. We define a parameter $\epsilon\equiv V_0^2/V_c^2-1$ as a measure of the dimensionless distance from the onset of EC at V_c. The voltage had a stability of better than 10^{-4} V, which is less than 1/20 of the smallest voltage step. At each

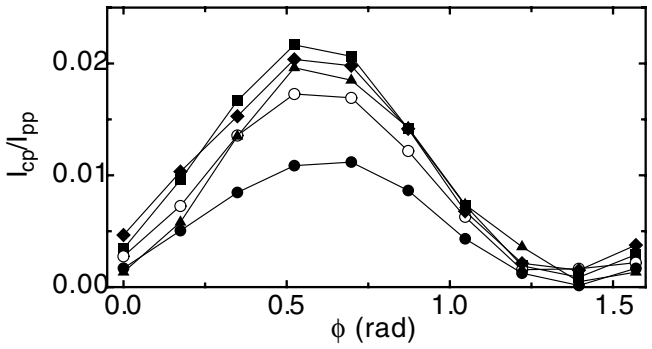

FIG. 1. The ratio of the transmitted intensity I_{cp} with polarizers crossed at 90° relative to each other to the intensity I_{pp} with parallel polarizers, as a function of the angle of orientation ϕ of the crossed-polarizer pair and for $V_0=0$. For the origin of ϕ we chose the orientation of one of the straight edges of the sample. Open circles: no cell. Solid circles: MBBA with DMOAP. Solid diamonds: Phase 5A-1. Solid squares: MBBA with polyimide (this cell was not used further in this work). Solid up-triangles: MBBA-4. The area used was about 1.23×1.23 mm^2.

V_0, we waited 600 s and then took 256 images $\tilde{I}_i(\mathbf{x},\epsilon)$ [$\mathbf{x}=(x,y)$ denotes the coordinates in the plane of the sample]. Near onset the time interval between images was 5 s, yielding nearly uncorrelated images; however, the time interval was reduced to 0.15 s for the construction of the space-time images used in the study of traveling waves. For the Phase 5A samples the images had a physical size of 284×284 μm^2 and were digitized with a spatial resolution of 200×200 pixels using 4096 gray levels. A typical image above V_c for Phase 5A is shown in Fig. 2(a). The stripes in the pattern correspond to somewhat disordered convection rolls. For the MBBA samples the sizes of the images were 1.2×1.2 mm^2 and the images had a spatial resolution of 360×360 pixels. Examples are shown in Figs. 3(a) and 3(c). In this case we found oblique rolls at low [Fig. 3(a)] and normal rolls at high [Fig. 3(c)] driving frequency. In the oblique case the structure factor [Fig. 3(b)] contained two pairs of peaks with the same k but different θ. For all other MBBA cells only normal rolls were found.

The image-analysis method was described in detail elsewhere [39,40]. Briefly, each image was normalized with a background image in the form of $I_i(\mathbf{x},\epsilon)=\tilde{I}_i(\mathbf{x},\epsilon)/\tilde{I}_0(\mathbf{x},\epsilon)-1$. Here $\tilde{I}_0(\mathbf{x},\epsilon)$ is the average of all 256 images. For each $I_i(\mathbf{x},\epsilon)$ the structure factor $S_i(\mathbf{k},\epsilon)$ (the square of the modulus of the Fourier transform) was calculated and 256 $S_i(\mathbf{k},\epsilon)$ were averaged to obtain $S(\mathbf{k},\epsilon)$. Here $\mathbf{k}=(k_x,k_y)$ is the wave vector of the pattern and the length is scaled by the sample spacing d. An example of a structure factor is shown in Fig. 2(b). The relatively weak central peak corresponds to fluctuations of the Freedericksz domain and was filtered out in further analysis of EC. Below V_c it was the only contribution to the power and it was used to find the Freedericksz transition at V_F. The outermost two azimuthally extended peaks are the second harmonics of the EC pattern and were also filtered out. The two strongest peaks are from the fundamental components of the EC pattern. The existence of only one

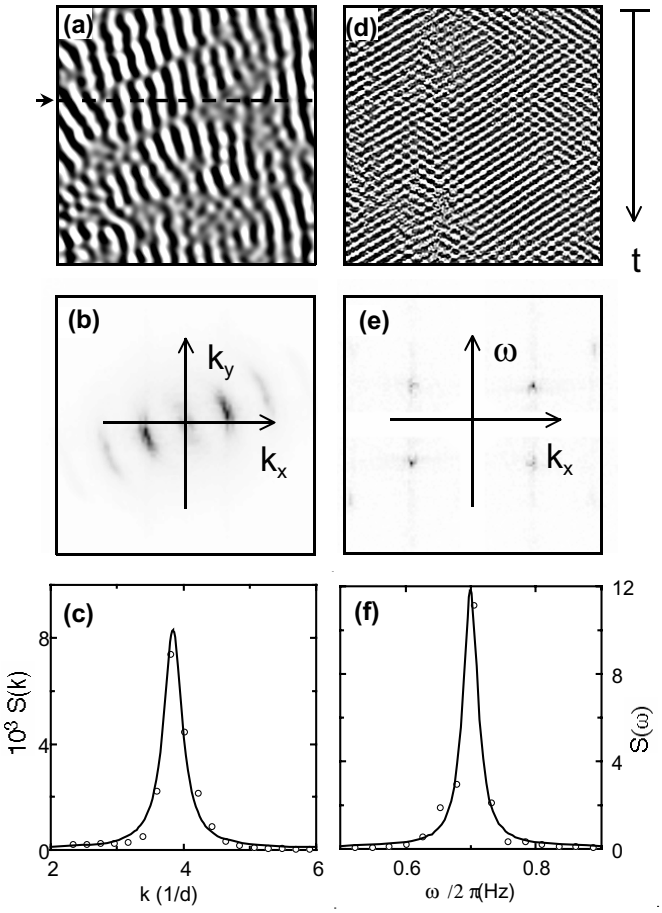

FIG. 2. (a) A shadowgraph image (a snapshot, after image division and Fourier filtering) covering an area of 0.28×0.28 mm^2 for $f=500$ Hz and $\epsilon=0.005$ from sample Phase 5A-1. The dashed horizontal line indicates the selected row for the construction of the space-time image shown in (d). It is parallel to one of the edges of the sample corresponding to $\phi=0$. Its direction is chosen as the x axis in further discussions. (b) the structure factor $S(\mathbf{k},\epsilon)$ over the range $-13\lesssim(k_x,k_y)\lesssim13$ of images like (a), averaged over 256 images. (c) the azimuthal average $S(|k|)$ of (b). The solid line is a fit of a Lorentzian function to the data. (d) the shadowgraph intensity along the dashed horizontal line in (a) as a function of time, for a width of 0.36 mm and for $0\lesssim t\lesssim38.4$ s. (e) The structure factor $S(k_x,\omega)$ obtained from (d), covering $-2.6\lesssim\omega/2\pi\lesssim2.6$ Hz and $-13\lesssim k_x\lesssim13$. (f) the average $S(\omega)$ of $S(k_x,\omega)$ over k_x in (e). The solid line is a fit of a Lorentzian function to the data.

such pair of peaks shows that the pattern consists of normal rolls, and the significant azimuthal extent of these peaks reflects the disorder in the pattern. The distance of the maximum of the strongest peaks from the origin gives $k_p=\sqrt{k_x^2+k_y^2}$ and the orientation of this maximum yields the angle $\theta=\tan^{-1}(k_y/k_x)$ of the roll pattern relative to the camera frame. For normal rolls this angle should coincide with the bend direction of the Freedericksz domain. The total power P of the EC pattern is obtained by integrating the structure factor over the relevant area in k space. A radial structure factor $S(k)$, as shown in Fig. 2(c), was obtained by taking an azimuthal average of Fig. 2(b). A fit of $S(k)=S_0/[\xi_0^2(k-k_p)^2+1]$ to the data is shown in Fig. 2(c) and was used to determine k_p.

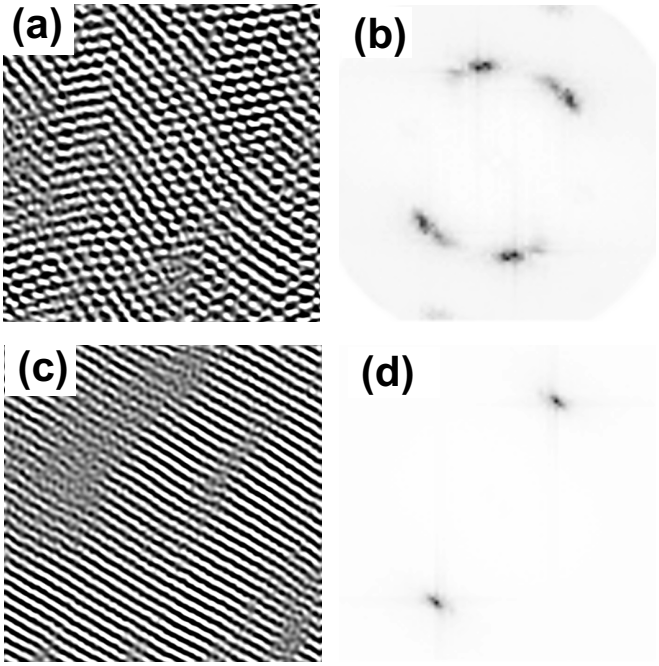

FIG. 3. Images from sample MBBA-4. (a) and (b) are a shadowgraph image and its structure factor at $f=20$ Hz and $\epsilon=0.005$. (c) and (d) are a shadowgraph image and its structure factor at $f=100$ Hz and $\epsilon=0.005$. The images cover an area of 1.21×1.21 mm^2 and the structure factors are for $-9.2\lesssim(k_x,k_y)\lesssim9.2$. The orientation is as in Fig. 2.

The traveling nature of the convection rolls was analyzed by using space-time images [38,40] that consist of the time evolution in the vertical direction of a particular horizontal line in the real-space image. Figure 2(d) is the space-time image corresponding to the horizontal dashed line in Fig. 2(a). One sees that the pattern consists of rolls traveling in both directions. Figure 2(e), $S(k_x,\omega)$, is the modulus squared of the Fourier transform of the space-time image, Fig. 2(d). The traveling frequency ω can be readily derived from the fit of a Lorentzian function to the average $S(\omega)$ of $S(k_x,\omega)$ over k_x, as shown in Fig. 2(f).

The experimental results for the Freedericksz voltage and for various parameters at the onset of EC will be compared with theoretical predictions. The evaluation of the predictions requires a knowledge of numerous fluid properties as input. We collected the values used by us [28,38] in Table II.

TABLE II. Properties of Phase 5A [38] and MBBA [28] used in the evaluation of theoretical predictions.

Parameters	Phase 5A (30 °C)	MBBA (25 °C)
Conductivities		
$\sigma_\parallel/\sigma_\perp$	1.69	1.50
Dielectric constants		
$\epsilon_\parallel$	5.033	4.72
$\epsilon_\perp$	5.217	5.25
Viscosity coefficients (10^{-3} N s/m^2)		
α_1	−39	−18.1
α_2	−109	−110
α_3	1.5	−1.1
α_4	56.3	82.6
α_5	82.9	77.9
α_6	−24.9	−33.6
Elasticity constants (10^{-12} N)		
k_{11}	9.8	6.66
k_{22}	4.6	4.2
k_{33}	12.7	8.61

III. FREEDERICKSZ TRANSITION

Figure 4 shows the total power P as a function of V^2 at $f=500$ Hz for Phase 5A-1. Only fluctuations near $k=0$ are contributing. Thus the power is quite small, as can be seen by comparison with the EC power in Fig. 7 below. However, it increases sharply near $V^2=66$ V^2. This increase identifies the Freedericksz transition. Using a straight-line fit to the data slightly above the transition we found $V_F=8.132$ V. Consistent with the theoretical prediction $V_F^\infty=\pi\sqrt{k_{33}/(\epsilon_0|\epsilon_a|)}$ and previous experiments [3,5,41], V_F was independent of the driving frequency f [see Fig. 9(a) below]. As found by others, [5,41] its value was about 7% below the theoretical value. A similar shift, by about 8%, was found for sample MBBA-4. These differences are larger than the possible errors due to the uncertainties of the fluid properties used in the theory, and we attribute them primarily to weak anchoring. In the theory perfect strong anchoring is assumed; i.e., the director is taken to be orthogonal to the glass-NLC interface even when the Freedericksz domain forms above V_F. For real samples one expects a downward threshold shift corresponding to $V_F/V_F^\infty<1$ that depends on the parameter combination dG/k_{33} where G is the anchoring energy per unit area and k_{33} is an elastic constant [42]. With $V_F/V_F^\infty\simeq0.93$ as found in the experiment, one finds

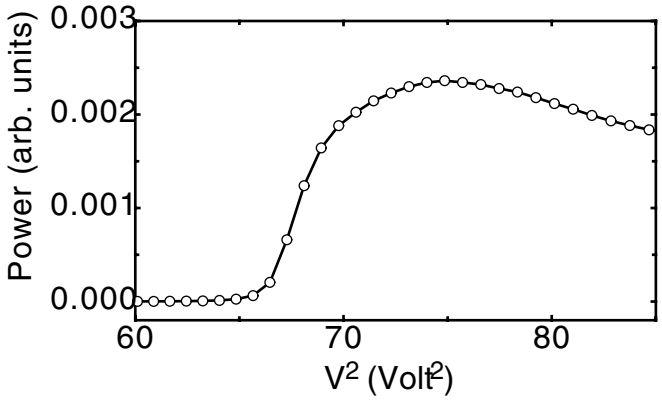

FIG. 4. The fluctuation power P, in arbitrary units, of the shadowgraph signal as a function of V^2 at $f=500$ Hz for sample Phase 5A-1. For this work a single polarizer was used. There is a sudden rise of P at the Freedericksz transition.

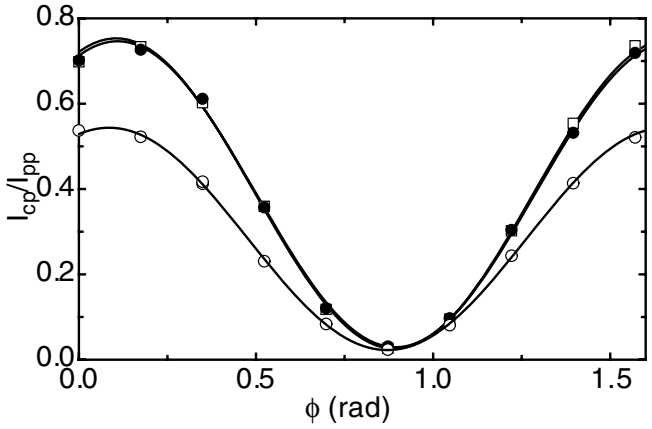

FIG. 5. The ratio of the transmitted intensity I_{cp} with polarizers crossed at 90° relative to each other to the intensity I_{pp} with parallel polarizers as a function of the angle of orientation ϕ of the crossed-polarizer pair. An area of about 1.34×1.34 mm^2 was used. The data are for MBBA-4. Open squares: $f=100$ Hz and $V_0=4.30$ V. The voltage is well above $V_F=3.90$ V and well below the onset of EC at $V_c=9.99$ V. Solid circles: $f=200$ Hz and $V_0=4.30$ V. Open circles: $f=200$ Hz and $V_0=21.36$ V (at 200 Hz $V_c=33.50$ V). The solid lines are fits of $I_{cp}/I_{pp}=I_0+\delta\sin[4(\phi-\phi_0)]$ to the data that yielded ϕ_0 = 1.28, 1.29, and 1.26 rad for open squares, solid circles, and open circles, repectively. The domain orientation is given by the location of the minima and thus is equal to $\theta_d=\phi_0-\pi/8$. In all three cases the minimum of I_{cp}/I_{pp} was found to be close to 0.025.

$G\simeq1\times10^{-5}$ N/m. This is in the range of typical values for homeotropic anchoring [43]. Another possible source of a reduced V_F is a pretilt of the director (i.e., an alignment that is not perfectly orthogonal to the surfaces). This is expected to lead to an imperfect bifurcation, possibly leading to an effective threshold shift. In view of the results in Fig. 1 we expect this shift to be small, but it may contribute somewhat to a reduction of the measured V_F.

Results for V_F for all samples are given in Table I. As mentioned above, for MBBA-4 (which was prepared with Polyimide coating) V_F is about 8% below the theoretical value. The MBBA samples with DMOAP coatings have considerably lower transition voltages, suggesting that the anchoring for this coating is significantly weaker.

Above V_F a single Freedericksz domain was attained after initial transients died out [41,44]. Visual evidence for the single-domain structure was found in the spatial uniformity of the shadowgraph images. More quantitatively, we show in Fig. 5 the ratio between the transmitted intensity with crossed polarizers to that with parallel polarizers, as was done for $V=0$ in Fig. 1. One sees that the ratio came remarkably close to zero when the crossed-polarizer orientation ϕ coincided with the domain orientation θ_d. This could not have happened if different parts of the sample were occupied by domains of different orientation. As found by others [19], for a given sample the domain orientation θ_d was always the same from one run to another, indicating that it was chosen from among the infinity of ideally degenerate orientations by some minor azimuthal inhomogeneity. We rotated a sample in the laboratory frame and found that the domain orientation rotated with the sample, thus ruling out any influence for instance from prevailing magnetic fields. Some results for θ_d are shown in Fig. 6. As one would expect, the data show that the domain orientation was independent of the drive frequency and of the drive voltage.

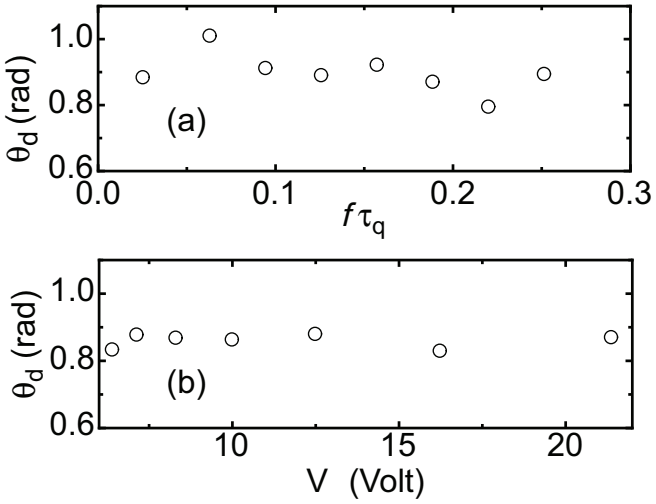

FIG. 6. (a) The domain orientation θ_d above V_F for MBBA-4 as a function of the dimensionless drive frequency $f\tau_q$ ($\tau_q=1.26\times10^{-3}$ s is the charge relaxation time) for $V_0=4.30$ V. (b) The domain orientation above V_F for MBBA-4 as a function of the drive voltage V_0 for a drive frequency of 200 Hz.

IV. ONSET OF ELECTROCONVECTION

A. Nature of the bifurcation

Data for the total shadowgraph power P of sample Phase 5A-1 near the transition to EC are shown in Figs. 7(a) and 7(b) [the central peak of $S(\mathbf{k})$ due to the Freedericksz-domain fluctuations was filtered out before P was calculated]. Data were recorded at $f=500$ Hz first with increasing (squares) and then with decreasing (circles) voltage. For samples with planar alignment hysteresis had been observed over some parameter ranges [26,34] and was indicative of a subcritical bifurcation. For the data in the figure there is a slight shift of the circles relative to the squares that is noticeable near onset, but it is in a direction opposite to that expected for hysteresis and we attribute it to a small drift during the 35 h that elapsed between the two measurements of the onset. Thus the results do not reveal hysteresis and are consistent with a supercritical bifurcation. In Fig. 7(b) the data near the bifurcation are shown with greater resolution as a function of ϵ. The data with increasing and decreasing V_0 had been fitted separately by straight lines, and the fits had yielded $V_c=9.883$ and 9.896 V for increasing and decreasing V_0 respectively.

B. Sample stability

Figure 8(a) gives the results for $V_c(t)$ of sample Phase 5A-1 over a long time period (the second and third points from the left are the data from Fig. 7). This cell was over a year old, and we do not know the origin of the small drift that can be represented well by the straight-line fit

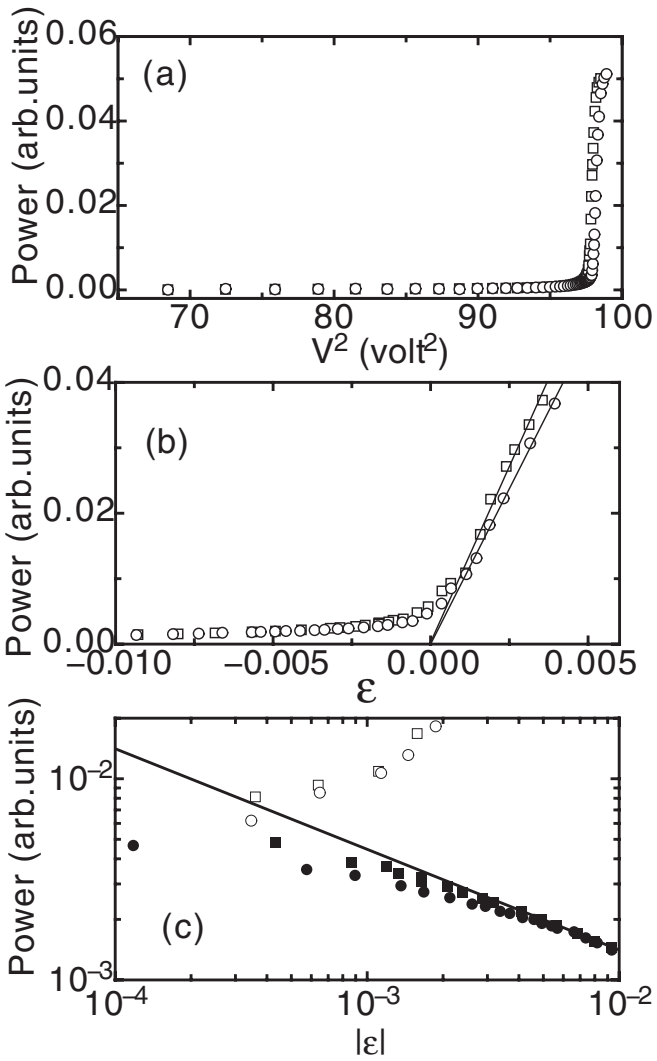

FIG. 7. (a) The power P as a function of V_0^2 at $f=500$ Hz for sample Phase 5A-1. The arbitrary scale of P is the same as that in Fig. 4. The squares and circles correspond to increasing and decreasing voltages, respectively. (b) the power P as a function of $\epsilon \equiv V_0^2/V_c^2 - 1$ near the onset of EC at V_c. The squares and circles correspond to increasing and decreasing voltages, respectively. The solid lines are the straight-line fits to the data slightly above the threshold. (c) The power as a function of the absolute value of ϵ on logarithmic scales. The squares and circles correspond to increasing and decreasing voltages, respectively. Solid symbols: $\epsilon<0$. Open symbols: $\epsilon>0$. The solid line corresponds to a power law with an exponent of $-1/2$.

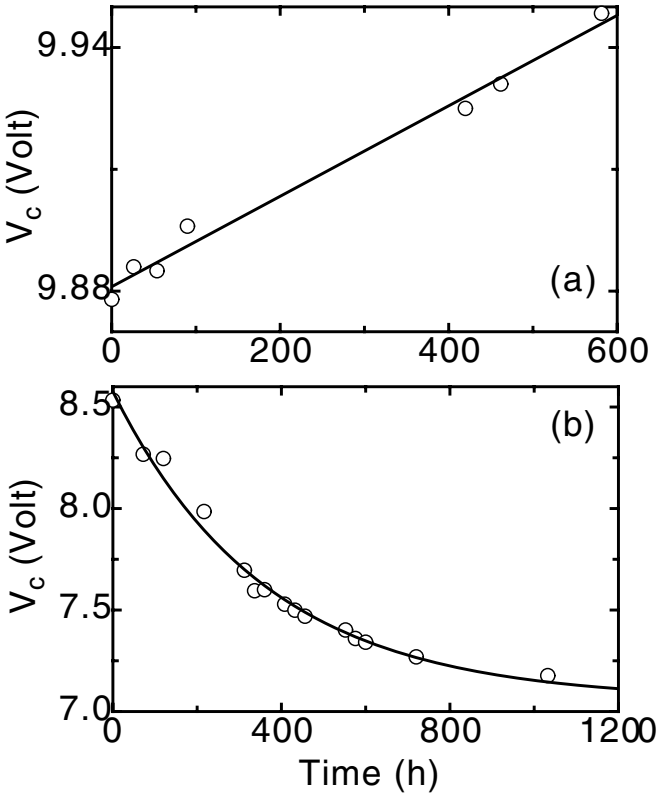

FIG. 8. (a) The critical voltage V_c as a function of time for sample Phase 5A-1 at $f=500$ Hz. The solid line is a straight-line fit to the data. The third and fourth data points from the left correspond to results in Fig. 7. (b) The critical voltage V_c as a function of time for sample MBBA-4 at $f=50$ Hz. The solid line is a fit of an exponential function to the data. For this sample the conductance was measured at $t=120$ and 1032 h and found to be 3.4×10^{-8} and 5.6×10^{-8} $(\Omega\mathrm{m})^{-1}$, respectively.

$V_c(t)=9.881+1.1\times10^{-4}t$ V with t in hours. Values of V_c used in the analysis of the experiments were based on this fit. The drift is small compared to the frequency dependence of V_c reported below.

For MBBA we found a larger drift of V_c early in the life of a cell, but the drift slowed down exponentially in time. This is shown for MBBA-4 and $f=50$ Hz in Fig. 8(b) where the results can be represented by $V_c(t)=1.52\exp(-t/\tau)+7.06$ V with $\tau=363$ h. Measurements on this cell were started soon after it was built, and a likely explanation of this transient may be found in impurity diffusion from the periphery of the cell into the interior and an associated increase of the conductance. Indeed, we found an increase of $\sigma_\parallel$ from $3.4\times10^{-8}\ \Omega^{-1}\,\mathrm{m}^{-1}$ at $t=120$ h to $5.6\times10^{-8}\ \Omega^{-1}\,\mathrm{m}^{-1}$ at $t=1032$ h. Here too the fitted function was used to determine V_c. Again the drift was small compared to the frequency dependence of V_c. All further MBBA results reported below are based on MBBA cells that had been aged for about a month or more.

C. Fluctuations

The "rounding" of the supercritical bifurcation due to fluctuations is apparent particularly in Fig. 7(b). The solid lines indicate the extrapolation to $V_c(t)$ (i.e., to $\epsilon=0$) of the data above the bifurcation. In Fig. 7(c) we show the fluctuation power, as a function of $|\epsilon|$ on logarithmic scales. Within the approximation of linear theory [(LT)—i.e., of the Gaussian model] one expects a power-law divergence with an exponent of 1/2 [solid line in Fig. 7(c)]. The data agree with this prediction near $|\epsilon|=0.01$, but begin to fall below it already for $|\epsilon|\lesssim0.004$. For the real system a power law cannot continue all the way to $\epsilon=0$ because the power must remain finite at onset. Thus a deviation is expected qualitatively, but it is surprising to see it at such large $|\epsilon|$ values because on the

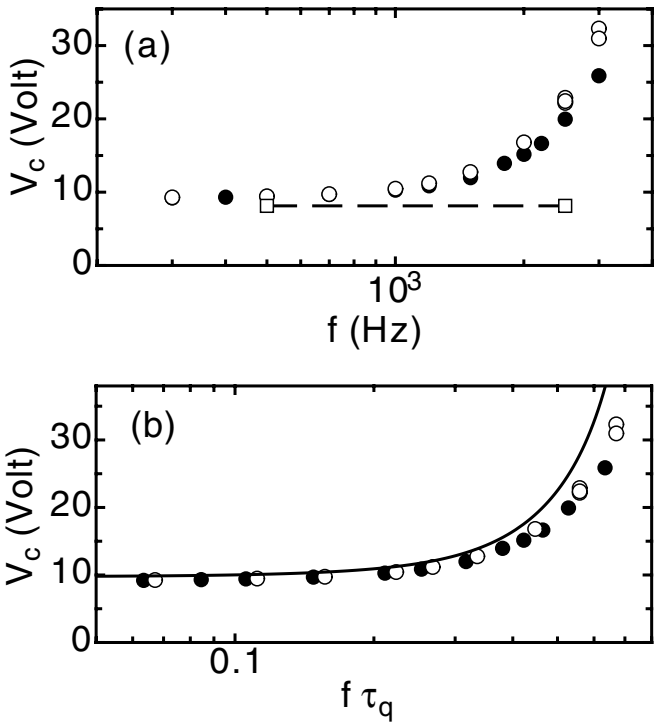

FIG. 9. (a) The critical voltage V_c as a function of the driving frequency f for samples Phase 5A-1 (solid circles) and Phase 5A-2 (open circles). The open squares and the dashed line show the Freedericksz voltage V_F. (b) The critical voltage V_c as a function of the dimensionless driving frequency $f\tau_q$ for the same samples as in (a). The solid line is the theoretical prediction [28].

basis of the effective thermal noise intensity the crossover to the critical region is expected to occur near $|\epsilon| = 10^{-4}$.

D. Pattern at onset

Although a quantitative study of the patterns near onset is beyond the scope of this paper, we mention that they are chaotic in space and time. Spatiotemporal chaos at the onset of EC had been predicted by Hertrich *et al.* [28] in the case of a stationary bifurcation and seen experimentally by Richter *et al.* [19,30]. Theoretically it was discussed further by Rossberg *et al.* [45,46] for stationary bifurcations. In that case it is associated with the Goldstone mode [28] that arises from the degeneracy of the orientation of the Freedericksz domain of the ideal sample. Various aspects of these patterns, including their evolution at larger ϵ, have been discussed in a number of papers [5,23–25,31]. For most of the present samples the onset of EC took the form of a Hopf bifurcation, leading to a chaotic state that is dominated by the dynamics of domain walls between right- and left-traveling waves, which to our knowledge differs from the nature of the chaos observed previously. We illustrate this by a movie [47] for Phase 5A-1 with $f = 1000$ Hz and $\epsilon = 0.003$ that runs at a speed corresponding to real time when displayed at 30 frames per second. Details of these chaotic patterns will be discussed in a subsequent paper [48].

E. Critical voltage V_c

The critical voltage V_c as a function of the driving frequency f for samples Phase 5A-1 and Phase 5A-2 is plotted in Fig. 9(a). As expected, V_c increases monotonically with increasing f, as found before for planar [38] and homeotropic [5] alignments. There is a small difference of $V_c(f)$ between the two samples which we attribute to the small difference of the conductances (see Table I).

The properties at onset have been explored theoretically [28] within the framework of the SM [2,3] of EC. For homeotropic alignment the problem is more complicated than it is for the planar case because the ground state, consisting of the domain that formed after the Freedericksz transition, is spatially inhomogeneous in the direction perpendicular to the confining plates. It must first be calculated numerically. Nonetheless, to a good approximation the dependence of V_c on $\sigma_\parallel$ can be removed by scaling the frequency with the charge relaxation time $\tau_q = \epsilon_0 \epsilon_\perp / \sigma_\perp$. For this purpose we obtained $\sigma_\perp$ from our measured $\sigma_\parallel$ and $\sigma_\parallel / \sigma_\perp = 1.69$ [38] (see Table II). In Fig. 9(b) we show V_c as a function of $f\tau_q$ for both cells. The data can be represented well by a single curve. The solid line in Fig. 9(b) is based on the stability analysis, carried out numerically, of the Freedericksz state below the EC transition [28]. The results obtained using the properties of Phase 5A-1 or Phase 5A-2 are indistinguishable from each other within the resolution of the figure. As can be seen, they are in quite good agreement with the data, although the theory gives slightly higher values at large $f\tau_q$. A similar difference between theory and experiment was found before [5]. It is unclear whether one can attribute this difference to small errors in the fluid properties used in the evaluation of the theoretical prediction. Near-perfect agreement between theory and experiment can be obtained by calculating τ_q for the experimental points using a value of $\sigma_\parallel$ that is about 13% larger than its measured value.

For the four MBBA samples V_c is plotted as a function of f in Fig. 10(a). In this case the conductance varies over a wide range and the dependence of V_c on f differs a great deal for different samples. However, again the data collapsed within their experimental uncertainty onto a single curve when plotted against $f\tau_q$, as shown in Fig. 10(b). It is interesting to note that the difference of about 20% between the V_F values for the cells prepared with DMOAP and polyimide (see Table I) does not seem to noticeably influence V_c. It seems that V_c is far enough above V_F so that there remains very little influence of the director anchoring at the surface on the director field as a whole which at this point has assumed a near-planar configuration. The theoretical result for V_c is shown as a solid line in the figure. It agrees very well with the data at small $f\tau_q$ but is a little low at higher frequencies. Even over the large range of $\sigma_\perp$ covered by the MBBA cells, the predictions for the highest and lowest $\sigma_\perp$ are almost indistinguishable within the resolution of the figure. Previous experiments using MBBA [30,31] achieved better agreement between theory and experiment, but in that work the conductance of the sample was unknown and chosen [31] so as to achieve this agreement. For the present data near-perfect agreement between theory and experiment can be achieved by calculating τ_q for the experimental points using a value of $\sigma_\parallel$ that is about 25% smaller than its measured value.

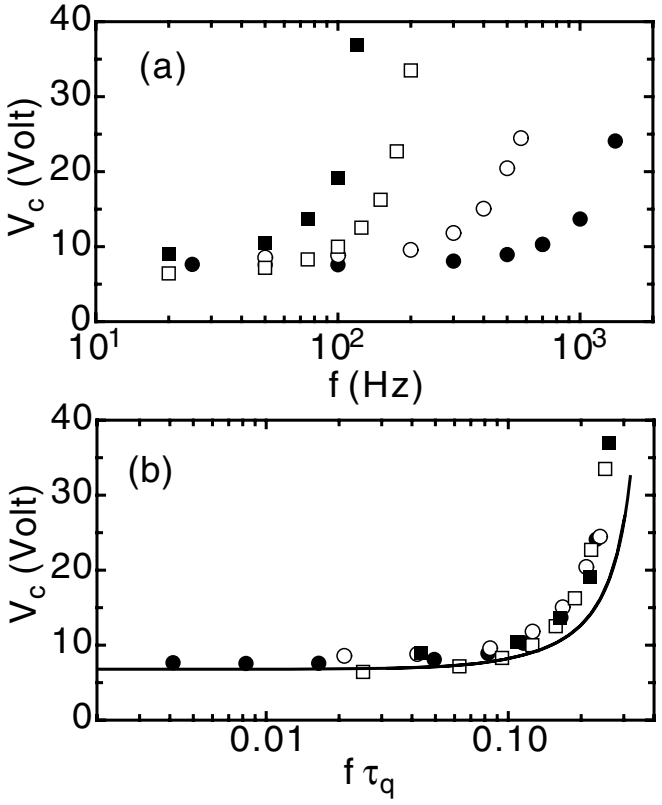

FIG. 10. (a) The critical voltage V_c as a function of the driving frequency f for samples MBBA-1 (solid circles), MBBA-2 (open circles), MBBA-3 (solid squares), and MBBA-4 (open squares). (b) The critical voltage V_c as a function of the dimensionless driving frequency $f\tau_q$ for the same samples as in (a). The solid line is the theoretical prediction [28].

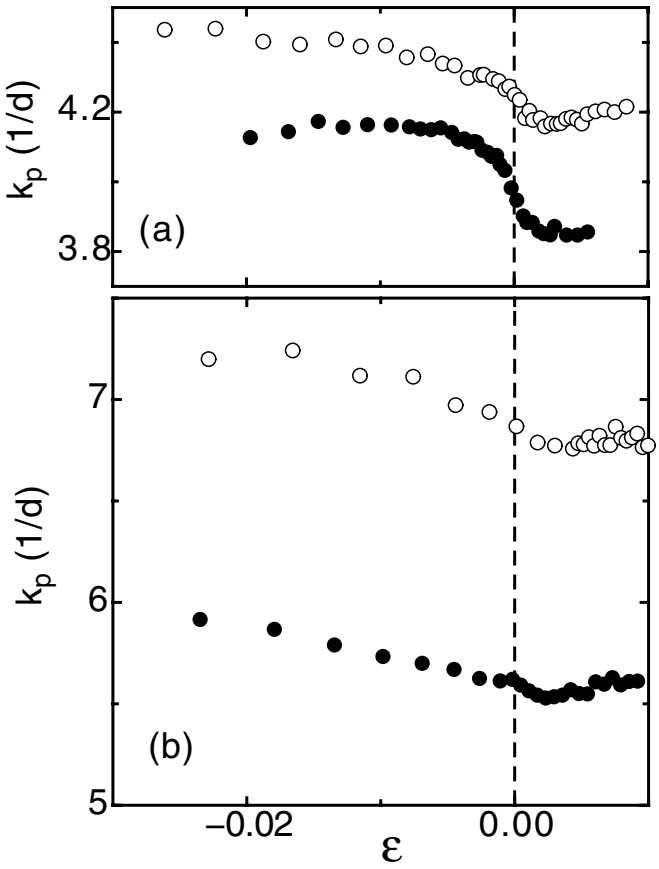

FIG. 11. (a) The peak wave number k_p as a function of ϵ for sample Phase 5A-1 at $f=500$ Hz (solid circles) and $f=1000$ Hz (open circles). (b) k_p as a function of ϵ for sample MBBA-4 at $f=20$ Hz (solid circles) and $f=100$ Hz (open circles).

F. Critical wave number k_c

Examples of experimental results for the wave number k_p at the maximum of $S(k)$ [see Fig. 2(c)] near the onset of EC are shown as a function of ϵ for Phase 5A-1 in Fig. 11(a) and for MBBA-4 in Fig. 11(b). For $\epsilon<0$ the results are for the fluctuations below the onset of convection. The decrease of k_p with increasing ϵ below onset for MBBA is similar to what was found for the NLC I52 with planar alignment [40]. For Phase 5A the ϵ dependence near onset is surprisingly strong particularly at the lower frequency. For both materials the ϵ dependence is stronger than would be expected from the maximal linear growth rates [40] suggesting an influence of fluctuation interactions on the wave numbers. In all cases k_p is continuous at $\epsilon=0$ and passes through a minimum just above onset. Here we are concerned with the value $k_c=k_p(\epsilon=0)$ at onset, but recognize that the fluctuation-induced anomalous ϵ dependence of k_p may have reduced that value by several percent below the classical value that would be obtained by extrapolating the results well below onset to $\epsilon=0$ and that would be predicted from the linear growth rates.

In Fig. 12(a) we show the results for k_c as a function of frequency for Phase 5A. The two samples yielded slightly different results. As shown in Fig. 12(b), a difference of about 15% remains after plotting the data as a function of $f\tau_q$. The origin of this remains unclear. An error in the cell spacing d (which sets the length scale used to calculate k) for one or the other of the samples is probably not the problem. An adjustment of d would spoil the excellent scaling of the Hopf frequency ω_c which is proportional to d^{-3} [see Sec. IV H and Fig. 18(b) below]. At low frequencies the results for Phase 5A-1 are in excellent agreement with the prediction of the theory [28] which is shown as a solid line in Fig. 12(b). However, this excellent agreement may be somewhat illusory because, as mentioned above, the experimental values are reduced below the deterministic value by the fluctuations; the effect of the fluctuations is not considered in the deterministic theoretical calculations [28]. At higher frequencies the theory departs somewhat from the Phase 5A-1 data. Very good agreement can be achieved by calculating τ_q for the experimental points using a value of $\sigma_\parallel$ that is about 13% larger than its measured value, as was the case for V_c of this sample; but the vertical offset of the Phase 5A-2 data remains unexplained.

The k_c results for MBBA are shown in Fig. 13. In this case much larger differences remain between the several samples even when the data are plotted against $f\tau_q$ as in Fig. 13(b). Presumably one can attribute these differences to variations of the homeotropic anchoring strength. Indeed MBBA-4, which has the highest Freedericksz-transition voltage and thus presumably the strongest anchoring, has the

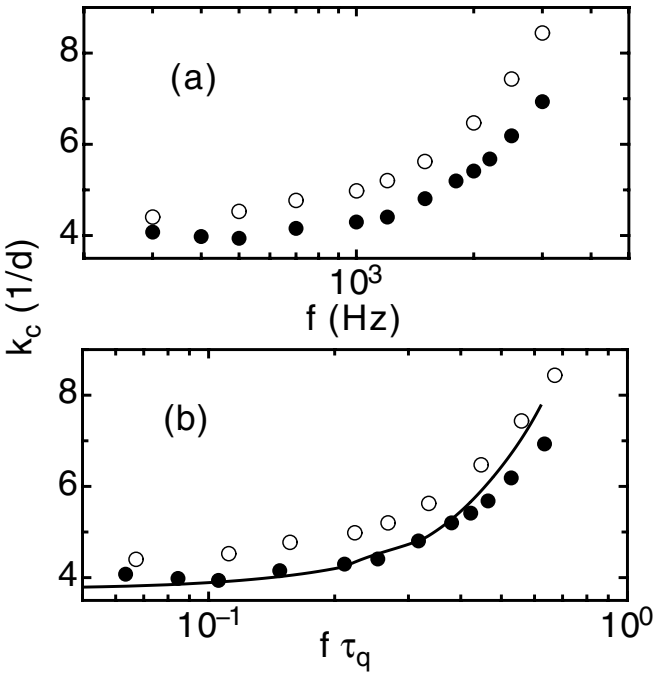

FIG. 12. (a) The critical wave number k_c as a function of the driving frequency f for samples Phase 5A-1 (solid circles) and Phase 5A-2 (open circles). (b) The critical wave number k_c as a function of the normalized driving frequency $f\tau_q$ for the same samples of (a). The solid line is the theoretical prediction [28].

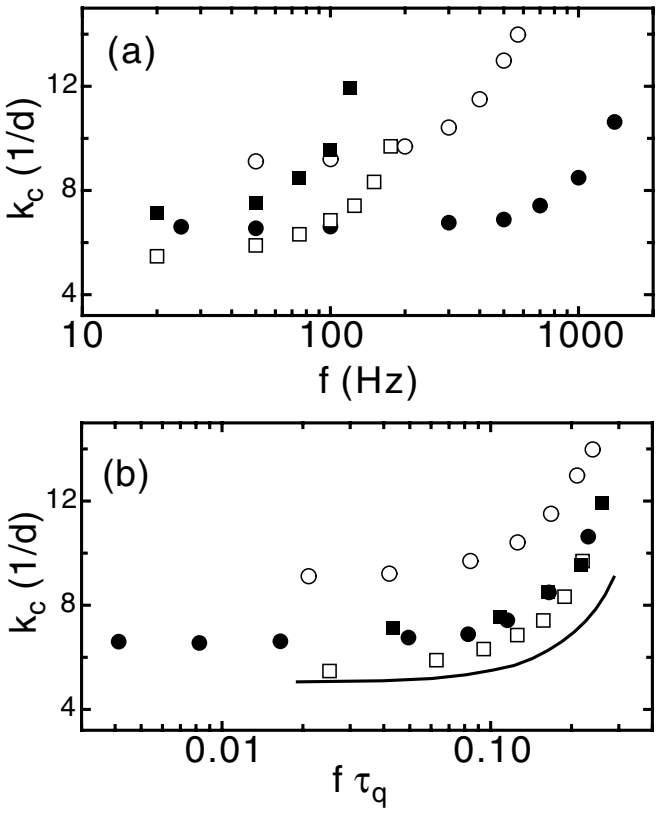

FIG. 13. (a) The critical wave number k_c as a function of the driving frequency f for samples MBBA-1 (solid circles), MBBA-2 (open circles), MBBA-3 (solid squares), and MBBA-4 (open squares). (b) The critical wave number k_c as a function of the normalized driving frequency $f\tau_q$ for the same samples of (a). The solid line is the theoretical prediction [28].

lowest k_c when the data are plotted as a function of $f\tau_q$. The theoretical prediction for k_c [28] is also shown in Fig. 13(b). The difference between the MBBA-4 results and the prediction is in the same direction as but a bit larger than the difference observed for V_c; see Fig. 10. Here too the theory could be brought into better agreement with experiment by changing the value of $\sigma_\perp$ used to calculate τ_q for the experimental points. We emphasize that the seemingly reasonable agreement between MBBA-4 and theory should be viewed with caution because the theory does not consider the change of k_c due to fluctuation interactions.

G. Critical obliqueness angle θ_c

Understanding the orientation of the convection rolls presents a significant problem. In this section we present results for the roll orientations of samples Phase 5A-1, Phase 5A-2, and MBBA-4. Let us consider first Phase 5A. As shown in Fig. 2(b), the structure factor (SF) consisted of only two well-defined peaks at angles θ and $\theta+\pi$ at all driving frequencies, corresponding clearly to a single dominant fluctuation orientation. One would thus expect that the prevailing mode corresponded to normal rolls. However, near but below the onset of EC θ changed with ϵ, as shown in Fig. 14(a). Since the Freedericksz-domain orientation was independent of V_0 for $V_0 < V_c$, it appears that the fluctuation wave vector was not strictly aligned with the domain. Above onset the orientation of the wave vector was more nearly ϵ independent. The results for $\theta_c = \theta(\epsilon=0)$ are shown in Fig. 15 as solid circles. They are found to be drive-frequency independent, consistent with a unique average orientation above onset that was aligned with the Freedericksz-domain orientation.

For Phase 5A the theory [28] with the material parameters in Table II, translated vertically to agree with the measurements at high and low f, yields the solid line in Fig. 15. At high and low frequencies normal rolls are predicted, but over an intermediate frequency range terminating in two Lifshitz points oblique rolls (OR's) are expected. Previous experiments with Phase 5A had confirmed the existence of the OR range [5,49–51,51]. However, in the present experiment there was no evidence for OR's at any frequency. Because of this difference between the present measurements on the one hand and theory as well as earlier experiments on the other, we show in Fig. 15 (as open circles) also the results for θ_c from sample Phase 5A-2. They also show only normal rolls. When plotted as a function of $f\tau_q$, the theoretical result is not sensitive to $\sigma_\parallel$, and thus it predicts oblique rolls in nearly the same range for the two samples as shown by the dashed curve. We do not know the reason for the absence of OR's in our measurements, but note that the work from Ref. [49] was done with a sample of somewhat smaller $\sigma_\parallel$ (the value of $\sigma_\perp$ needed to get agreement between the theoretical and experimental Lifshitz frequencies corresponded to $\sigma_\parallel \simeq 1.5\times10^{-7}\ \Omega^{-1}\ \mathrm{m}^{-1}$). Perhaps more relevant is that our samples were relatively thin, with $d \simeq 12\ \mu$m, whereas those

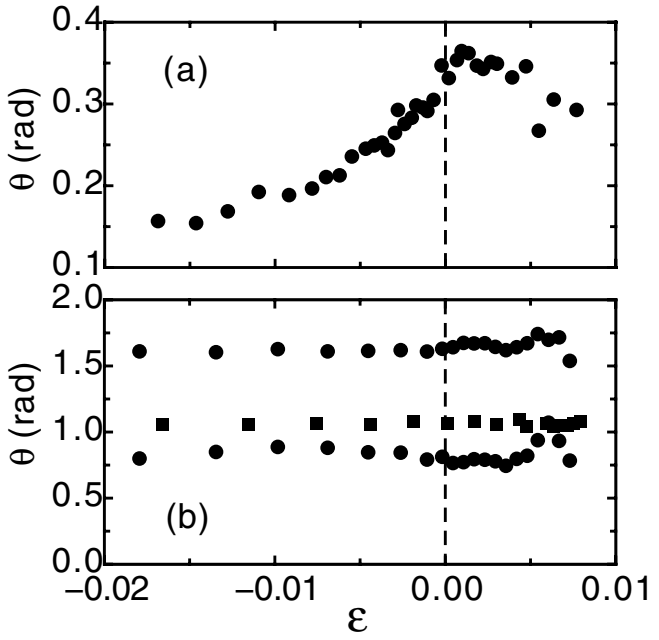

FIG. 14. (a) The obliqueness angle θ as a function of ϵ for sample Phase 5A-1 at $f=500$ Hz. (b) The obliqueness angle θ as a function of ϵ for sample MBBA-4 at $f=20$ Hz (solid circles) and $f=100$ Hz (solid squares).

used in Refs. [49] to [51] had $26 \lesssim d \lesssim 46$ μm.

Below onset the data for MBBA are in one sense easier to understand. Here a pair of peaks occurs in the SF at angles θ_1 and θ_2, as shown by the solid circles in Fig. 3(b). One would assume that the peaks correspond to two sets of degenerate oblique rolls with orientation $(\theta_2-\theta_d)=\pi-(\theta_1-\theta_d)$ where θ_d is the domain orientation. Consistent with this assumption, the two angles are ϵ independent within measurement error, as shown by the data in Fig. 14(b). However, they yield the results for θ_c shown as solid circles in Fig. 16. Also shown in that figure, as open circles, are the domain orientations θ_d measured below V_c. One sees that one of the supposedly

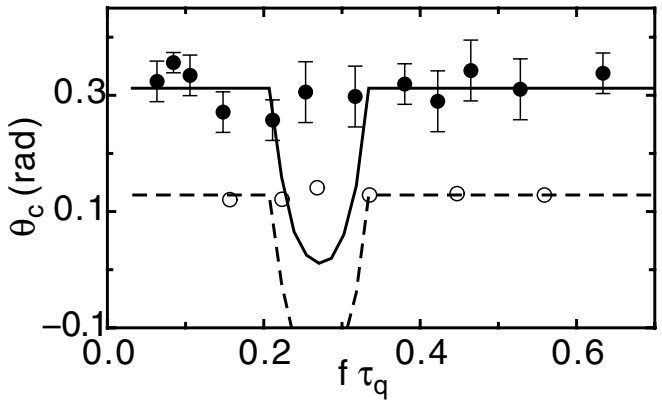

FIG. 15. (a) The critical angle θ_c as a function of the normalized driving frequency $f\tau_q$ for sample Phase 5A-1 (solid circles) and sample Phase 5A-2 (open circles). The solid and dashed lines are the theoretical prediction [28] shifted vertically so as to march the data at small and large f.

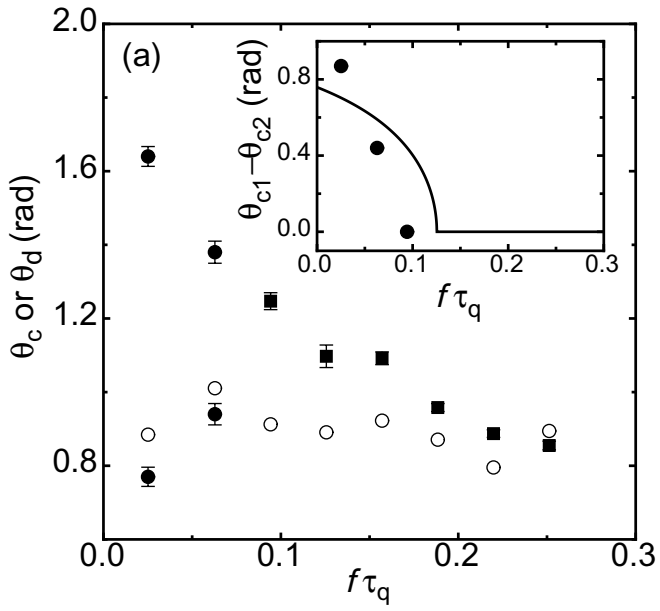

FIG. 16. The critical angle θ_c as a function of the normalized driving frequency $f\tau_q$ for MBBA-4. Solid circles: θ_{c1} and θ_{c2} of oblique rolls. Solid squares: θ_c of "normal" rolls. For comparison, the domain direction θ_d from Fig. 6(a) measured at $V_0=4.302$ V is shown again as open circles. In the inset, the difference angle $\theta_{c2}-\theta_{c1}$ is shown as solid circles and the solid line is the theoretical result [28].

degenerate oblique rolls has nearly the same orientation as the Freedericksz domain, while the other differs from θ_d by about twice the presumed angle of obliqueness. In other words, there are two modes that (within experimental resolution) acquire a positive growth rate simultaneously at V_c, and within experimental resolution one is aligned with the orientation of the Freedericksz domain, while the other is at an oblique angle to that domain. We have no explanation for this unexpected result, but conjecture that it is associated with the Goldstone mode of this system.

The difference between the two roll orientations is shown as solid circles in the inset of Fig. 16. These results agree reasonably with the theoretical prediction [28] which is shown as a solid line, but of course in the theory the two modes have degenerate orientations relative to the Freedericksz director field. The data show that the obliqueness angle vanishes at a Lifshitz frequency $f_L\tau_q \simeq 0.1$.

For $f>f_L$ only a single mode prevails for MBBA-4. The measured orientation θ of that mode is shown as a function of ϵ by the solid squares in Fig. 14(b). It is ϵ independent, but one sees that it does not fall halfway between the low-frequency results for the oblique modes (solid circles). This asymmetry can be seen also by comparing Figs. 3(b) and 3(d). It illustrates the unexpected misalignment between the rolls and the Freedericksz domain. The critical value θ_c for this single-mode regime is shown in Fig. 16 as solid squares. One sees that the misalignment relative to the Freedericksz domain persists also above f_L. Alignment of the roll vector with the domain orientation is achieved only as $f\tau_q$ increases to about 0.2.

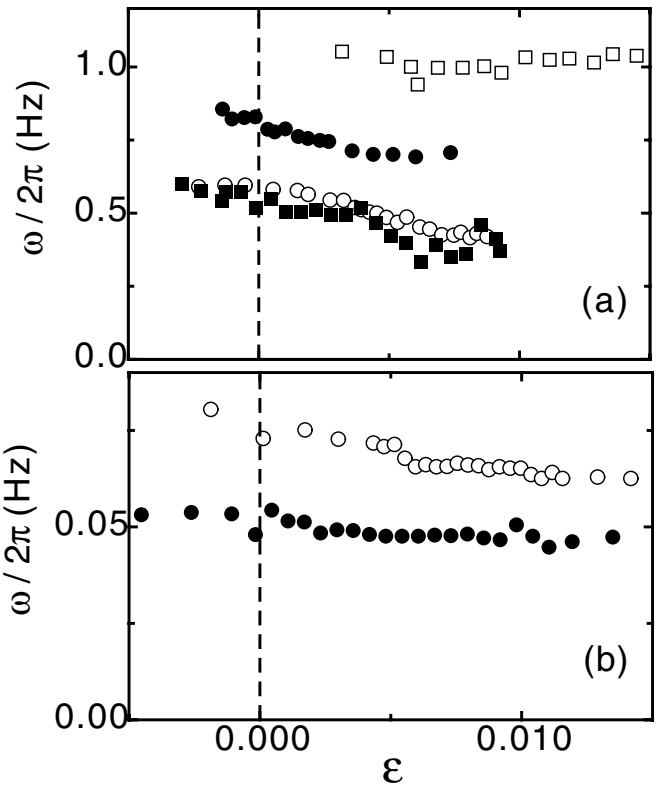

FIG. 17. (a) The traveling frequency ω as a function of ϵ for sample Phase 5A-1 at $f=500$ Hz (solid circles), $f=1000$ Hz (open circles), $f=1800$ Hz (solid squares), and $f=3000$ Hz (open squares). (b) The traveling frequency ω as a function of ϵ for sample MBBA-4 at $f=20$ Hz (solid circles) and $f=100$ Hz (open circles).

H. Hopf frequency ω_c

For the Phase 5A samples and for MBBA-3 and MBBA-4 a space-time plot like Fig. 2(d) revealed the presence of traveling waves (TW's) near the onset of EC. Using the SF $S(k_x,\omega)$ [Fig. 2(e)] and a fit of a Lorentzian function to its average $S(\omega)$ [Fig. 2(f)] we determined the frequencies ω of the TW. Results as a function of ϵ at several drive frequencies f for Phase 5A-1 [MBBA-4] are shown in Fig. 17(a) [Fig. 17(b)]. The high-conductance samples MBBA-1 and MBBA-2 (see Table II) yielded a stationary bifurcation to EC.

For negative ϵ the measured frequencies are those of the TW fluctuations. It is notable that $\omega(\epsilon)$ in each case varies continuously through $\epsilon=0$. This again confirms the supercritical nature of the bifurcation. Because of nonlinear dispersion a subcritical bifurcation usually leads to a jump in ω [34].

The results for the Hopf frequency ω_c (i.e., of ω at $\epsilon=0$) of Phase 5A are shown in Fig. 18(a) as a function of f. The two samples yield results that differ by about 15% at small f and by about 50% at large f. For MBBA-3 and MBBA-4 the ω_c data are given in Fig. 19(a) as open and solid squares. They differ dramatically from each other, with the higher-conductance sample MBBA-4 yielding the lower values. Consistent with this trend, no TW were ever observed for MBBA-1 and MBBA-2.

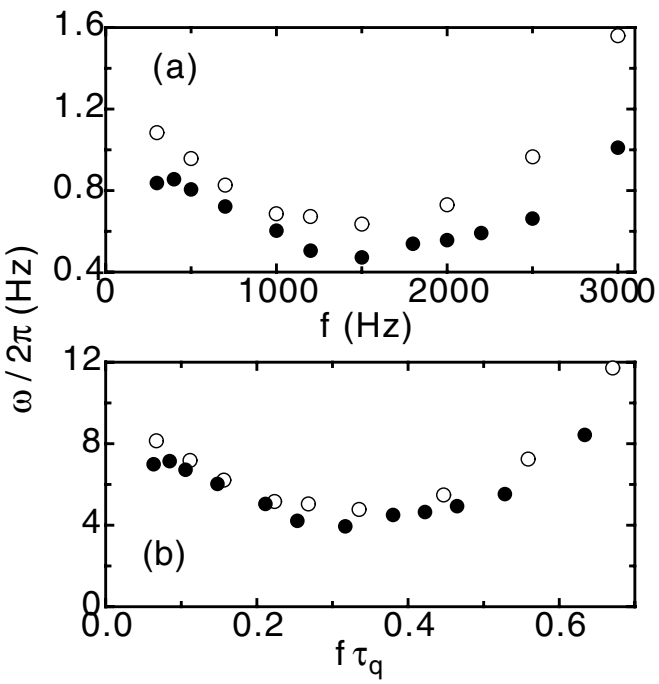

FIG. 18. (a) The Hopf frequency ω_c as a function of the driving frequency f for samples Phase 5A-1 (solid circles) and Phase 5A-2 (open circles). (b) The reduced Hopf frequency $\omega_r \equiv 10^{19}\omega_c\sigma_\perp^{1/2}d^3$ as a function of the dimensionless driving frequency $f\tau_q$ for the same samples of (a).

Also shown in Fig. 19(a), as stars, plusses, and crosses, are the results from Ref. [19]. For those measurements the sample conductance was not recorded. However, we expect that a higher conductance leads to a higher value of f where V_c diverges (the "cutoff" frequency). The cutoff frequencies for the samples of Ref. [19] suggest that the trend of a lower ω for a higher conductance is valid also for those data.

The standard model of EC assumes an ohmic conductivity and always predicts stationary bifurcations. In order to remedy this shortcoming, the WEM was introduced [3,33]. It permits dissociation and recombination of ions and considers the ionic mobilities. It has been remarkably successful in explaining the observed Hopf frequencies in samples with planar alignment quantitatively [20,38]. At this time the WEM has not yet been developed for the homeotropic case. However, one would expect that the differences between the planar and homeotropic cases are mainly at the quantitative level (for more details, see the following subsection) and that the trends with parameters are largely the same. For the planar case the WEM predicts [3,20,38] that, over wide parameter ranges, ω_c should be approximately proportional to $1/d^3$ and to $1/\sqrt{\sigma_\perp}$. Thus, as was done in Refs. [20,38] for the planar case, we show in Figs. 18(b) and 19(b) the reduced frequency $\omega_c\sigma_\perp^{1/2}d^3$ as a function of $f\tau_q$. For both Phase 5A and for MBBA we see that the data collapse on a unique curve for each substance.

I. Comparison with planar convection

We mentioned already in the Introduction that central features of homeotropic convection can be understood in terms

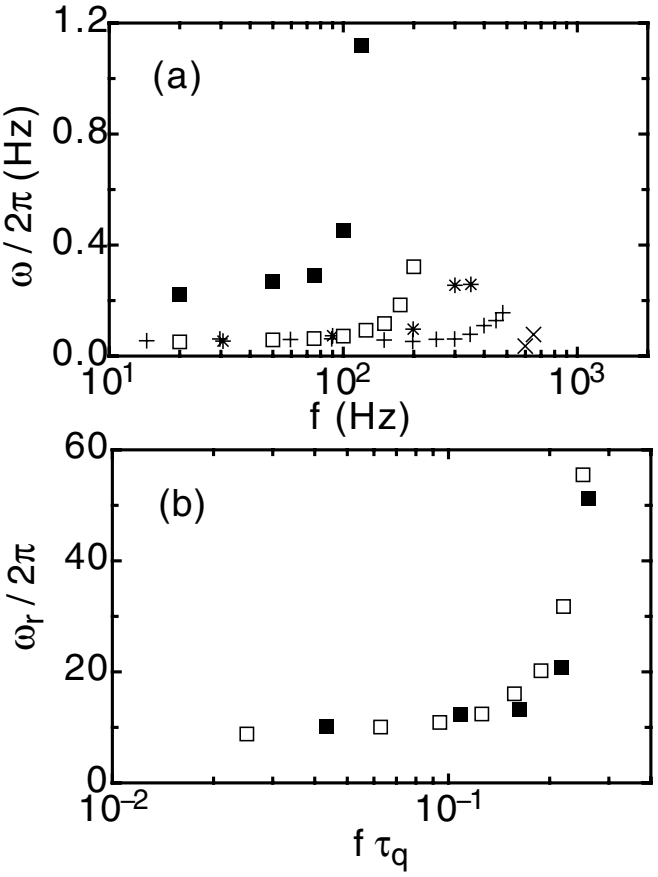

FIG. 19. (a) The Hopf frequency ω_c as a function of the driving frequency f for samples MBBA-3 (solid squares) and MBBA-4 (open squares). The results labeled (a), (b), and (c) in Fig. 7 of Ref. [19] are shown as stars, pluses, and crosses, respectively. (b) The reduced Hopf frequency $\omega_r \equiv 10^{19}\omega_c\sigma_\perp^{1/2}d^3$ as a function of the dimensionless driving frequency $f\tau_q$ for samples MBBA-3 (solid squares) and MBBA-4 (open squares).

of convection in a planar layer that expands from the midplane towards the confining plates with increasing voltages $V_0 > V_F$. The theoretical considerations given in this section are based on the standard model.

The situation is very transparent for MBBA, on which we mainly concentrate. In the homeotropic configuration the Freedericksz transition takes place at $V_F = 4.25$ V. At low frequencies it is followed by the EC bifurcation at $V_c \simeq 6.81$ V. Here numerical calculations show that the planar layer at the midplane already fills 65% of the cell (as an approximate measure for the width of this layer, we take the average $\langle n_x \rangle$ of the planar component n_x of the director over the cell thickness). With increasing f the critical voltage for the homeotropic case $V_c^h(f)$ increases monotonically and tends to diverge near the cutoff frequency $\tau_q f_c \approx 0.35$ (see Fig. 10). The corresponding prediction for the critical voltage $V_c^p(f)$ of *planar* convection as a function of the frequency starts at $V_c^p(0) = 6.58$ V and grows steeply as well as f_c is approached, while the ratio $V_c^p(f)/V_c^h(f)$ remains practically unchanged at about 1.07 ± 0.03 for the whole frequency range. Thus it is evident that the homeotropic convection is mainly governed by the planar convection mechanism of the underlying planar layer. It seems not to be important that the width of this layer expands with increasing voltage as well. At larger voltages it fills nearly 90% of the cell and the remainder corresponds to homeotropic boundary layers. Consistent with our picture of homeotropic convection as planar convection in a layer thinner than the cell thickness d, we found the critical wave numbers in the planar case always to be about 10% smaller than the homeotropic ones.

The above reasoning in principle applies to Phase 5A as well. However, in this case $V_F = 8.76$ V is larger than the MBBA value, while $V_c^p(0) = 5.42$ V is lower. At the onset of homeotropic convection $[V_c^h(0) = 9.76]$ the planar layer fills only 50% of the cells and the ratio $V_c^h(f)/V_c^p(f)$ approaches the MBBA value 1.07 from above at larger f, when the planar layer expands.

The analysis of V_c and q_c is expected to be relevant also for a Hopf bifurcation at threshold. According to the WEM [3,29,33] V_c and q_c differ very little from the SM prediction for the planar case. This is in agreement with experiments on MBBA [16], Phase 5 [38], and I52 [20]. Due to the close analogy between planar and homeotropic convection discussed above, the SM should work very well for q_c and V_c in the homeotropic case as well and this has been confirmed in this paper. For the same reason the scaling properties of ω_c derived and confirmed experimentally in the planar case [20,38] should hold in homeotropic convection. This also has been convincingly demonstrated in this paper.

V. SUMMARY

In this paper we presented the results of a detailed quantitative investigation of the properties of two different homeotropically aligned nematic liquid crystals near the bifurcation to electroconvection. We used two different samples of the NLC Phase 5A, and four different samples of MBBA. Particularly the MBBA samples covered a wide range of conductance; this range was achieved by different doping levels.

An optical study both below and above the Freedericksz transition at V_F confirmed that monodomain samples prevailed and established the domain orientation θ_d. A determination of V_F yielded results slightly smaller than the theoretical value based on the fluid properties, suggesting that the homeotropic anchoring, although perfect (i.e., perpendicular to the glass surface), was not perfectly rigid.

We measured the power (or variance) P of the fluctuations below onset and of the pattern above onset to confirm that the bifurcations to EC were supercritical. The measurements below onset revealed that the dependence of P on the distance ϵ from threshold agreed well with the linear-theory prediction $P \sim |\epsilon|^{-1/2}$ near $|\epsilon| = 0.01$, but (as expected) approached a constant value at $\epsilon = 0$ for smaller $|\epsilon|$.

The remainder of the paper was devoted to measuring the critical bifurcation parameters for the EC onset. These parameters included the critical voltage V_c, the critical wave number k_c, the critical angle of orientation θ_c of the roll wave vector relative to the domain orientation θ, and the traveling-wave frequency ω_c in the cases where the bifurcation was to a time-periodic state.

Theory suggests that an important time scale in EC is the charge relaxation time τ_q. We found that the results for V_c, when plotted against the dimensionless frequency $f\tau_q$, fell on a unique curve for a given NLC. This curve was in very good, but not perfect, agreement with a numerical evaluation of the theoretical prediction by Hertrich *et al.* [28]. It is not clear at this time whether the small difference between theory and experiment can be attributed to errors in the fluid properties used to evaluate the theory.

The wave number k_p of the fluctuations below and the convection patterns above onset varied significantly with ϵ in the vicinity of the bifurcation, suggesting an influence of nonlinear fluctuation interactions. At V_c the wave numbers were determined as a function of drive frequency. Even when plotted as a function of $f\tau_q$, they tended to be somewhat higher than the theoretical prediction [28]. We suggest that this difference between theory and experiment may be due to a combination of weak-anchoring (the theory assumes rigid anchoring) and fluctuation effects.

Perhaps the most remarkable results are those for the roll orientation θ. For Phase 5A this orientation depended on the applied voltage. This was unexpected because the structure factor revealed only a single mode, presumably corresponding to "normal" rolls. One would have expected these rolls to have a wave vector that coincides with the orientation θ_d of the Freedericksz domain. For $V_0 < V_c$, θ_d did not depend on V_0. Thus we conclude that the rolls reorient themselves at an oblique angle relative to θ_d as ϵ changes near onset. Presumably this phenomenon is associated with the rotational invariance of the system at small V_0 and the associated Goldstone mode that is expected theoretically [45,46] near the onset of EC, but we are not aware of a detailed explanation. At onset the pattern had a unique orientation independent of the drive frequency.

The MBBA samples behaved differently. Their roll orientations were independent of ϵ within our resolution. However, the orientations relative to θ_d were unusual. At small drive frequencies, two pairs of peaks were observed in the structure factor, suggesting the existence of oblique rolls. A Lifshitz point was found near $f_L\tau_q=0.1$, with only a single pair of peaks remaining in the structure factor at larger $f\tau_q$. One of the oblique-roll modes was oriented so as to coincide within our resolution with θ_d, while the other assumed an oblique angle relative to it. Above f_L the orientation of the single remaining peak in the structure factor was dependent upon f and coincided with θ_d only at our largest drive frequencies.

We found Hopf bifurcations for both Phase 5A samples and for the two MBBA samples with the smaller conductances $\sigma_\parallel$. At large $\sigma_\parallel$ the bifurcation in MBBA was stationary. This is qualitatively consistent with the predictions of the weak electrolyte model [3,29,33], although so far the WEM has been developed only for planar alignment. For the planar case the WEM predicts that the Hopf frequency ω_c should be approximately proportional to $d^{-3}\sigma_\perp^{-1/2}$, depending in addition primarily on material properties of the particular NLC. For our homeotropic case we found that the data for $\omega_r \propto \omega_c d^3 \sigma_\parallel^{1/2}$, when plotted against $f\tau_q$, fell onto a unique line for each NLC. A calculation of this line for the homeotropic case has not yet been carried out.

We conclude that there is overall good agreement between experimental measurements and theoretical predictions for this system, but that there remain some interesting differences at the quantitative level.

ACKNOWLEDGMENTS

S.-Q.Z. wishes to thank X.-C. Xu for his help in the apparatus design. The work was supported by the U.S. National Science Foundation through Grant No. DMR02-43336 and by NATO through Grant No. CLG 973103. A.B. and N.E. acknowledge support of Hungarian research Grant No. OTKA-K61075.

[1] For a review, see, for instance, E. Bodenschatz, W. Pesch, and G. Ahlers, Annu. Rev. Fluid Mech. **32**, 709 (2000).
[2] L. Kramer and W. Pesch, Annu. Rev. Fluid Mech. **27**, 515 (1995).
[3] L. Kramer and W. Pesch, in *Pattern Formation in Liquid Crystals*, edited by A. Buka und L. Kramer (Springer-Verlag, Berlin, 1996).
[4] W. Pesch and U. Behn, in *Evolution of Spontaneous Structures in Dissipative Systems*, edited by F. H. Busse and S. C. Mueller (Springer, Berlin, 1998).
[5] Á. Buka, P. Tóth, N. Éber, and L. Kramer, Phys. Rep. **337**, 157 (2000).
[6] L. Kramer and W. Pesch, in *Physical Properties of Nematic Liquid Crystals*, edited by D. A. Dummur, A. Fukuda, and G. R. Luckhurst, Emis Datareview Series No. 25 (INSPEC, London, 2001).
[7] W. Zimmermann, in *Nematics: Mathematical and Physical Aspects*, edited by J.-M. Coron, J. M. Ghidaglia, and F. Helein, Vol. 332 of NATO Advanced Study Institute Series C (Kluver Academic, Dordrecht, 1991), p. 401.
[8] I. Rehberg, B. L. Winkler, M. de la Torre Juárez, S. Rasenat, and W. Schöpf, Festkoerperprobleme **29**, 35 (1989).
[9] See, for instance, L. M. Blinov, *Electro-Optical and Magneto-Optical Properties of Liquid Crystals* (Wiley, New York, 1983).
[10] See, for instance, P. G. de Gennes and J. Prost, *The Physics of Liquid Crystals* (Clarendon Press, Oxford, 1993).
[11] S. Kai and K. Hirakawa, Suppl. Prog. Theor. Phys. **64**, 212 (1978).
[12] R. Ribotta, A. Joets, and L. Lei, Phys. Rev. Lett. **56**, 1595 (1986).
[13] A. Joets, X. D. Yang, and R. Ribotta, Physica D **23**, 235 (1986).
[14] A. Joets and R. Ribotta, Phys. Rev. Lett. **60**, 2164 (1988).
[15] I. Rehberg, S. Rasenat, J. Fineberg, M. de la Torre Juárez, and V. Steinberg, Phys. Rev. Lett. **61**, 2449 (1988).
[16] I. Rehberg, S. Rasenat, and V. Steinberg, Phys. Rev. Lett. **62**, 756 (1989).

[17] M. Dennin, G. Ahlers, and D. S. Cannell, in *Spatio-Temporal Patterns*, edited by P. E. Cladis and P. Muhoray (Addison-Wesley, Reading, MA, 1994) p. 353.
[18] M. Dennin, D. S. Cannell, and G. Ahlers, Mol. Cryst. Liq. Cryst. Sci. Technol., Sect. A **261**, 377 (1995).
[19] H. Richter, Á. Buka, and I. Rehberg, Phys. Rev. E **51**, 5886 (1995); in *Spatio-Temporal Patterns in Nonequilibrium Complex Systems*, edited by P. E. Cladis and P. P. Palffy-Muhoray (Addison-Wesley, Reading, MA, 1995), p. 343.
[20] M. Dennin, M. Treiber, L. Kramer, G. Ahlers, and D. S Cannell, Phys. Rev. Lett. **76**, 319 (1996).
[21] M. Dennin, G. Ahlers, and D. S. Cannell, Science **272**, 388 (1996).
[22] M. Dennin, G. Ahlers, and D. S. Cannell, Phys. Rev. Lett. **77**, 2475 (1996).
[23] S. Kai, K.-i. Hayashi, and Y. Hidaka, J. Chem. Phys. **100**, 19007 (1996).
[24] Y. Hidaka, J.-H. Huh, K.-i. Hayashi, S. Kai, and M. I. Tribelsky, Phys. Rev. E **56**, R6256 (1997).
[25] Y. Hidaka, J.-H. Huh, K.-i. Hayashi, M. I. Tribelsky, and S. Kai, J. Phys. Soc. Jpn. **66**, 3329 (1997).
[26] M. Dennin, D. S. Cannell, and G. Ahlers, Phys. Rev. E **57**, 638 (1998).
[27] E. Bodenschatz, W. Zimmermann, and L. Kramer, J. Phys. (Paris) **49**, 1875 (1988).
[28] A. Hertrich, W. Decker, W. Pesch, and L. Kramer, J. Phys. II **2**, 1915 (1992).
[29] M. Treiber and L. Kramer, Phys. Rev. E **58**, 1973 (1998).
[30] H. Richter, N. Klöpper, A. Hertrich, and A. Buka, Europhys. Lett. **30**, 37 (1995).
[31] P. Tóth, Á. Buka, J. Peinke, and L. Kramer, Phys. Rev. E **58**, 1983 (1998).
[32] For a recent review of the dependence of EC on the director-orientation geometry and on the material parameters, see Á. Buka, N. Éber, W. Pesch, and L. Kramer, in *Self-Assembly, Pattern Formation, and Growth Phenomena in Nano-Systems*, edited by A. A. Golovin and A. A. Nepomnyashchy, Vol. 218 of NATO Science Series II: Mathematics, Physics, and Chemistry (Springer, Dordrecht, 2006), pp. 55–82.
[33] M. Treiber and L. Kramer, Mol. Cryst. Liq. Cryst. Sci. Technol., Sect. A **261**, 311 (1995).
[34] I. Rehberg, S. Rasenat, M. de la Torre Juarez, W. Schöpf, F. Hörner, G. Ahlers, and H. R. Brand, Phys. Rev. Lett. **67**, 596 (1991).
[35] J. R. deBruyn, E. Bodenschatz, S. Morris, S. Trainoff, Y.-C. Hu, D. S. Cannell, and G. Ahlers, Rev. Sci. Instrum. **67**, 2043 (1996).
[36] When a standard broadband dielectric mirror was used, then the difference in reflectivity for *p*-polarized and *s*-polarized light led to significant circular polarization of the reflected beam. Thus this mirror was replaced with one with aluminum coating overcoated with a dielectric. As seen in Fig. 1, there still remained a slight polarization of the reflected light.
[37] We used Nissan Chemical Inductries polyimide coating SE-1211.
[38] M. Treiber, N. Éber, Á. Buka, and L. Kramer, J. Phys. II **7**, 649 (1997).
[39] U. Bisang and G. Ahlers, Phys. Rev. E **60**, 3910 (1999).
[40] M. A. Scherer and G. Ahlers, Phys. Rev. E **65**, 051101 (2002).
[41] B. L. Winkler, H. Richter, I. Rehberg, W. Zimmermann, L. Kramer, and A. Buka, Phys. Rev. A **43**, 1940 (1991).
[42] K. H. Yang and C. Rosenblatt, Appl. Phys. Lett. **43**, 1 (1983). See Eq. (7) of this reference.
[43] A. A. Sonin, *The Surface Physics of Liquid Crystals* (Gordon and Breach, New York, 1995).
[44] A. Buka, M. de la Torre Juárez, L. Kramer, and I. Rehberg, Phys. Rev. A **40**, 7427 (1989).
[45] A. G. Rossberg, A. Hertrich, L. Kramer, and W. Pesch, Phys. Rev. Lett. **76**, 4729 (1996).
[46] A. G. Rossberg and L. Kramer, Phys. Scr. **T67**, 121 (1996).
[47] See EPAPS Document No. E-PLEEE8-74-078609 for an MPEG movie of patterns like that in Fig. 2(a), but for $f = 1000$ Hz and $\epsilon = 0.003$. For more information on EPAPS, see http://www.aip.org/pubservs/epaps.html.
[48] S.-Q. Zhou and G. Ahlers, Phys. Rev. E , (2006) (following paper).
[49] A. G. Rossberg, N. Éber, Á. Buka, and L. Kramer, Phys. Rev. E **61**, R25 (2000).
[50] N. Éber, A. G. Rossberg, Á. Buka, and L. Kramer, Mol. Cryst. Liq. Cryst. Sci. Technol., Sect. A **351**, 161 (2000).
[51] N. Éber, S. Németh, A. G. Rossberg, L. Kramer, and Á. Buka, Phys. Rev. E **66**, 036213 (2002).